Nano Energy (2014) 8, 183–195

Available online at www.sciencedirect.com

ScienceDirect

journal homepage: www.elsevier.com/locate/nanoenergy

RAPID COMMUNICATION

Heat-induced formation of porous and free-standing MoS_2/GS hybrid electrodes for binder-free and ultralong-life lithium ion batteries

Ronghua Wang, Chaohe Xu, Jing Sun*, Yangqiao Liu, Lian Gao, Heliang Yao, Chucheng Lin

The State Key Lab of High Performance Ceramics and Superfine Microstructure, Shanghai Institute of Ceramics, Chinese Academy of Sciences, 1295 Dingxi Road, Shanghai 200050, PR China

Received 10 March 2014; received in revised form 26 April 2014; accepted 16 May 2014
Available online 18 June 2014

KEYWORDS
Graphene;
Molybdenum disulfide;
Free-standing;
Binder-free;
Lithium ion batteries

Abstract
Flexible and free-standing MoS_2/GS films are constructed for the first time based on a novel heat-induced formation process, during which self-generated gaseous species successfully trigger the formation of porous structure, without the assistance of any templates or spacers. Graphene forms an open porous network, with few-layered MoS_2 uniformly grown on the surface of GS. The fascinating structure provides several attractive features as anode material, including efficient ion transport, high conductivity and good structure durability. When used as free-standing and binder-free electrodes for lithium-ion batteries, the optimized hybrid film with graphene content of 32% exhibits superior rate capability (994, 880, and 598 mAh g^{-1} at 0.5, 1, and 5 A g^{-1}, respectively) and outstanding cycling performance at high rates (retaining 100.6% of the initial capacity after 1000 cycles at 1000 mA g^{-1}). Importantly, the electrochemical reaction kinetics and interfacial behavior of the hybrid electrode are also in-depth investigated by EIS and morphological study. The work described here can be extended to prepare various porous graphene-based hybrid films, for the application in a broad range of LIBs, electrochemical capacitors, sensors, and catalysts.

Introduction

Although the performance of rechargeable lithium-ion batteries (LIBs) continues to improve, their energy density

*Corresponding author. Tel.: +86 21 52414301; fax: +86 21 52413122.
E-mail address: jingsun@mail.sic.ac.cn (J. Sun).

http://dx.doi.org/10.1016/j.nanoen.2014.05.009
2211-2855/

and cycle life remain insufficient for future applications in consumer electronics, electric vehicles and large-scale renewable energy storage [1,2]. In order to satisfy these demands, the development of novel electrode materials with higher charge capacity and longer cycle life are highly expected. As a typical layered transition-metal sulfide, MoS_2 has a structure similar to that of graphite, in which three stacked atom layers (S-Mo-S) are held together by van der Waals forces [3,4]. Such a structure is favorable for efficient reversible Li^+ intercalation/extraction, which enables MoS_2 to be a good electrode material [5]. However, the poor electric/ionic conductivity between two adjacent S-Mo-S sheets results in fast capacity fading and inferior rate capability. To date, many efforts have been devoted to solving this problem. One strategy is to enlarge its interlayer distance so as to provide sufficient space for ultrafast lithium ion intercalation [6,7]. The other one is constructing MoS_2/carbon hybrid structures to enhance electric conductivity and structural stability [2,8-13].

Graphene sheets (GS), with high conductivity, large specific surface area and superior mechanical properties, can provide a support for anchoring nanocrystals and work as a highly conductive matrix [14-18]. The integration of MoS_2 and graphene is quite favorable because their structural and morphological compatibility could enable better chemical and electrical synergistic effect, thus leading to improved lithium storage properties [2,4]. For example, Chen et al. synthesized MoS_2/GS by an L-cysteine-assisted hydrothermal method [8]. The composite exhibited a specific capacity of $\sim$1100 mAh g^{-1} at a current of 100 mA g^{-1}. Lee and coworkers prepared MoS_2/GS based on concurrent reduction of $(NH_4)_2MoS_4$ and GO by hydrazine in the presence of CTAB [2]. The composite delivered a capacity of 808 mAh g^{-1} after 100 cycles at 100 mA g^{-1}. In their work, surfactants or hydrazine reduction were required to control crystal morphology and reduce GO, respectively. Very recently, Guo et al. employed a combination of lithiation-assisted exfoliation process and hydrazine reduction technique to prepare MoS_2/GS and greatly improved the cycle life (915 mAh g^{-1} after 700 cycles) [11]. However, the lithiation-assisted exfoliation of bulk MoS_2 to MoS_2 nanosheets is complicated, time-consuming and hard to be scaled up. Therefore, the development of a facile, scalable and green method to prepare MoS_2/GS is highly required and remains a challenge. Additionally, in the previous work, electrodes were usually prepared with active materials and polymer binder for battery test. Polymer binder may block the diffusion channels of ion transportation and the outstanding electric performance of graphene had been significantly sacrificed [14,19-21]. Rational design and optimization of the electrode structure are believed to be essential to further improve the electrochemical performance of MoS_2/GS. However, there were few reports on this aspect.

Currently, free-standing and binder-free electrodes had been envisioned as a novel electrode structure which was superior to the conventional binder-enriched electrode [9,20,22]. An ideal free-standing and binder-free electrode should simultaneously satisfy many critical features including efficient ion transport, high conductivity, and structure durability [23,24]. However, aggregation and stacking problems are commonly observed in most free-standing graphene-based hybrid papers reported to date [23,25,26]. This resulted in an inefficient ionic transport within the macroscopic hybrid film and a modest improvement in lithium storage performance. Recently, macroporous graphene films were first prepared by using polystyrene (PS) colloidal particles as sacrificial templates, and MnO_2 [27] and Co_3O_4 [28] were subsequently deposited onto porous graphene surfaces. Although improved rate performance and stability were achieved, the whole process is complicated and time-consuming. The preparation of pore-enriched graphene-based hybrid films (especially for the layered materials) without assistance of any spacers or templates still remains a challenge, however, with few reports to date.

Herein, for the first time, we report the construction of porous and free-standing MoS_2/GS hybrid films based on a novel heat-induced process. The whole process is facile, scalable, green and highly reproducible, and thus superior to the existing approaches for MoS_2/GS composite powders fabrication. Graphene formed an open porous network, with few-layered MoS_2 uniformly grown on the surface of GS. Importantly, this is also the first demonstration that heat-induced self-generated gaseous species created porous structure within hybrid films, without the assistance of any spacers or templates. The hybrid film integrates several desirable design rationales for high-energy anode materials based on ultrathin MoS_2 nanosheets, 3D highly conductive network, and a porous structure. As free-standing and binder-free electrodes, the hybrid films manifested a high capacity (1276 mAh g^{-1} at 100 mA g^{-1}), superior rate capability (994, 880, and 598 mAh g^{-1} at 0.5, 1, and 5 A g^{-1}, respectively) and outstanding cyclic stability (no capacity loss after 1000 cycles at 1000 mA g^{-1}). At a super-high current density of 10000 mA g^{-1}, a high capacity of 552 mAh g^{-1} was achieved over ultralong-term cycling of 7500 cycles, with a capacity decay as low as 0.00127% per cycle. Such superior electrochemical performance has rarely been achieved in previous reported work on MoS_2/GS materials.

Experimental

Materials preparation

GO was prepared from graphite powder by the modified Hummers method. $(NH_4)_2MoS_4$ was added into GO dispersion. The reaction mixture was stirred at 35 °C for 12 h to form the Mo-based intermediate/GO complex, which was vacuum-filtered using Anodisc membrane filters (47 mm in diameter, 0.2 μm). After drying, free-standing and flexible Mo-based intermediate/GO hybrid films can be obtained after peeling off from the filter membrane. Finally, the hybrid papers were annealed in a gas mixture (Ar/H_2 = 90:10) at 800 °C for 2 h to obtain MoS_2/GS hybrid paper. To obtain optimal electrochemical performance, the weight ratio of $(NH_4)_2MoS_4$/GO was varied as 1:1, 2.5:1 and 5:1, respectively. Accordingly, the samples were named as MoS_2/GS-I, MoS_2/GS-II and MoS_2/GS-III, respectively. Detailed characterization was carried out on the optimized sample MoS_2/GS-II hereafter. A control sample of bare MoS_2 was prepared by the same process except without graphene.

Electrode preparation

MoS_2/GS hybrid papers were directly used as free-standing electrode without any binder or additive (denoted as MoS_2/GS). Two control electrodes (denoted as pure MoS_2 and P-MoS_2/GS) were prepared by mixing 80 wt% active material (pure MoS_2 and MoS_2/GS powder, respectively), 10 wt% conducting carbon black, and 10 wt% polyvinylidene fluoride binder in N-methyl-2-pyrrolidone. The homogeneous slurries were then pasted on copper current collector and dried under vacuum at 110 °C for 12 h.

Materials characterization

The morphology was characterized by transmission electron microscope (JEM-2100F, JEOL, Tokyo, Japan). The field-emission scanning electron microscope (FE-SEM) analysis was performed on JSM-6700F at an acceleration voltage of 10.0 kV. X-ray diffraction (XRD) was carried out on a D/max 2550 V X-ray diffraction-meter with Cu-Kα irradiation at λ=1.5406. Raman spectroscopy was recorded on a DXR Raman Microscope with 532 nm excitation length, Thermal Scientific Corporation, USA. X-ray photoelectron spectroscopy (XPS) analysis was conducted using twin anode gun, Mg Kα (1253.6 eV) (Microlab 310F Scanning Auger Microprobe, VG SCIENTIFIC LTD). The conductivity of MoS_2/GS hybrid paper was measured by a four-point probe method in the van der Pauw configuration with an Accent HL5500 system. N_2 adsorption/desorption isotherms were determined using a Micromeritics ASAP2010 Analyzer (USA).

Electrochemical measurements

Cyclic voltammetry (CV) was carried out in a voltage range of 0–3.0 V with a scan rate of 0.5 mV s^{-1}. The electrochemical impedance spectroscopy (EIS) measurements were carried out on the samples with a PARSTAT 2273, using a sine wave of 10 mV over a frequency range of 100 KHz–0.01 Hz. The electrochemical properties of the electrodes were characterized at room temperature. Li foil was used as the counter electrode. The electrolyte was 1 M $LiPF_6$ in a 50:50 w/w mixture of ethylene carbonate (EC) and dimethyl carbonate (DMC). Cell assembly was carried out in a glove box with the concentrations of moisture and oxygen below 1 ppm. The batteries were measured using a CT2001 battery tester.

Results and discussion

The porous and free-standing MoS_2/GS hybrid films were constructed for the first time based on vacuum filtration and a subsequent thermal reduction process (schematically shown in Figure 1). When $(NH_4)_2MoS_4$ and GO were mixed together, NH_4^+ would adsorb on the surface of GO via electrostatic interaction and hydrogen bonding [29], while MoS_4^{2-} was attracted by NH_4^+ to form GO-NH_4^+-MoS_4^{2-} complex. In other words, negatively charged MoS_4^{2-} and GO can be bridged together by the positively charged NH_4^+. The principle is similar with the method of preparing GO wrapped negatively charged metal oxide, by modifying metal oxide with positively charged amine [30–32]. During the prolonged stirring, MoS_4^{2-} will hydrolyze and condensate to form a series of Mo-based intermediate (polythiomolybdate species and so on) [33–35]. TEM images showed that Mo-based intermediate, in the form of tiny nanoparticles (<1 nm), was tightly and uniformed anchored on the surface of GO (see Supplementary information, Figure S1c and d). The formation of Mo-based intermediate can be confirmed by FTIR spectra (Figure S2c and d) that two new bands appeared at 522 and 527 cm^{-1} after reaction, corresponding to (S–S) vibrations [36,37]. As revealed by the deconvoluted Mo3p XPS spectrum of Mo-based intermediate/GO complex (Figure S2 and Table S1), 8.0% nitrogen element existed within the hybrid complex. This suggests that Mo-based intermediate and GO were continuously bridged by the positively charged NH_4^+. Importantly, the Mo-based intermediate/GO complex was still highly dispersed in water due to the mild reaction condition (30 °C). The zeta potential of the complex was measured to be -67 mV, demonstrating that the complex represents sufficient mutual repulsion to ensure colloidal stability [38]. This endows the complex with excellent film-forming ability. Here, when $(NH_4)_2MoS_4$/GO mass ratio ranged from 1:1, 2.5:1 to 5:1, the complex could easily self-assemble into free-standing films by vacuum filtration. Finally, the porous MoS_2/GS hybrid films were obtained by thermal reduction of Mo-based intermediate/GO hybrid films in hydrogen atmosphere (10% in Ar), during which the yielded gaseous species (such as NH_3, H_2S, H_2O, CO and CO_2, Figure S2) would separate its initial compact layered structure (Figure S3) and induce porous structure formation. The whole process is facile, scalable, green and highly reproducible, which is superior to the existing approaches for MoS_2/GS composite powders fabrication [2,8,11]. It is observed that the resulting MoS_2/GS film with a diameter of ~40 mm exhibited a metallic luster with a bumpy surface. The inset in Figure 1 shows a good flexibility of the hybrid film. In this study, the graphene contents were measured to be 51%, 32%, and 19% for MoS_2/GS-I, MoS_2/GS-II, and MoS_2/GS-III, respectively.

The XRD patterns are shown in Figure 2. The peaks of MoS_2/GS composite showed a crystalline structure similar to that of pure MoS_2, which can be assigned to hexagonal structured MoS_2 (JCPDS: 37-1492). Noteworthy, the (002) diffraction peaks of graphene were not detected, indicating GS were separated by MoS_2 layers. X-ray photoelectron spectroscopy (XPS) was performed to determine the chemical composition (Figure 3). The full XPS spectra of MoS_2/GS showed the C, O, Mo and S peaks (Figure 3a). The calculated atomic ratio of S to Mo element was 1.91, approaching the theoretical value of MoS_2. Furthermore, the Mo3d spectrum showed two peaks at 229.3 and 232.3 eV, assigned to the doublet $Mo3d_{5/2}$ and $Mo3d_{3/2}$ [39,40] (Figure 3b). The S2p spectrum was deconvoluted into two peaks at 162.3 and 163.5 eV, which can be attributed to the spin-orbit couple $S2p_{3/2}$ and $S2p_{1/2}$, respectively (Figure 3c) [40,41]. Noteworthy, the C/O ratio of GS was 9.3, indicating the deep reduction of GO [42]. Consequently, the conductivity of MoS_2/GS-II composite reached as high as 6075.7 S m^{-1}. This value was one magnitude higher than most of those reported graphene-based composites [14,43] (~100 S m^{-1} for Fe_3O_4/GS, 795 S m^{-1} for Co_3O_4/GS) and comparable to chemically reduced graphene oxide film (7200 S m^{-1}) [44]. It means graphene can serve as an efficient electrically

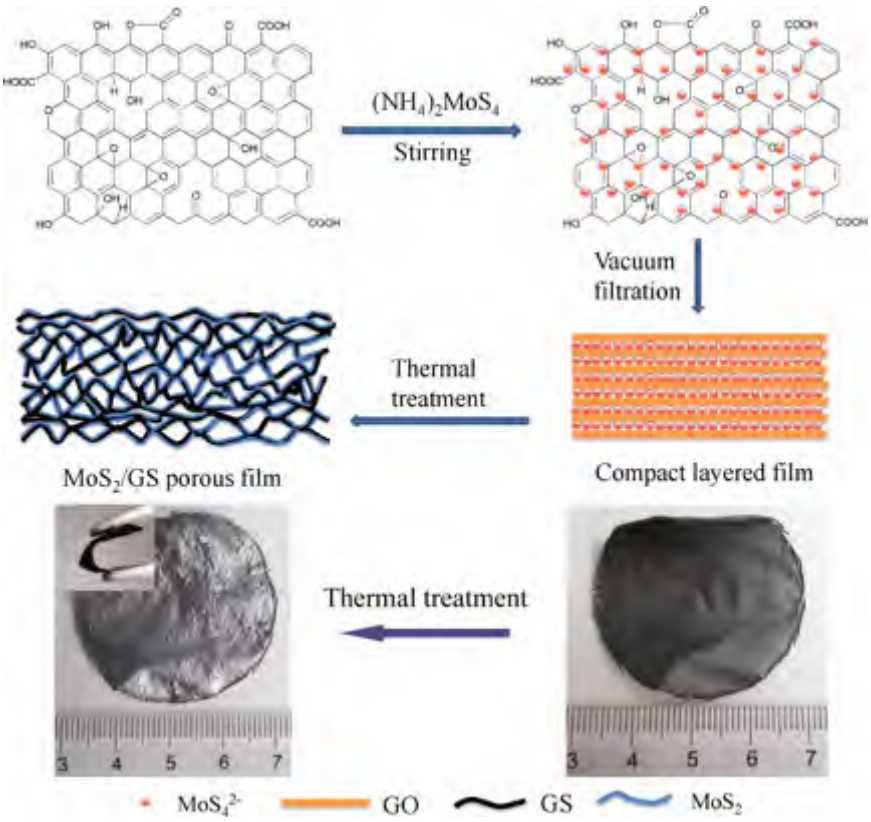

Figure 1 Schematic illustration of the synthesis of porous and free-standing MoS_2/GS hybrid films. The digital photographs show the transformation from Mo-based intermediate/GO film (right) to MoS_2/GS porous film (left) during thermal treatment. The inset shows a good flexibility of the MoS_2/GS porous film.

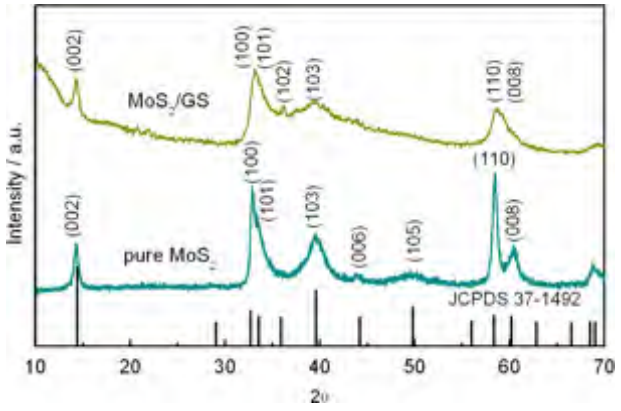

Figure 2 XRD curves of the as-synthesized MoS_2/GS hybrid film and pure MoS_2.

conducting network for fast electronic transport, which will result in high power density of the electrode. The above discussions confirmed the successful formation of highly conductive composite consisting of stoichiometric MoS_2 and deeply reduced GS.

Raman spectroscopy has been extensively used to characterize carbon materials. Moreover, it could be employed to identify the layer number of MoS_2. As shown in Figure 3d, the two peaks of pure MoS_2 at 376 and 403 cm^{-1} correspond to the E^1_{2g} and A_{1g} modes of the hexagonal MoS_2 crystal, respectively [2,4,45]. The spectra of MoS_2/GS revealed the characteristic peaks of MoS_2 at 379 and 401 cm^{-1} and the D and G bands of graphene. It has been reported that frequency difference between E^1_{2g} and A_{1g} decreased stepwise with the decreasing number of MoS_2 layers [46-48]. Here, the frequency difference of MoS_2/GS and pure MoS_2 was 22 cm^{-1} and 27 cm^{-1}, respectively. It is estimated that the average number of layers for MoS_2/GS was 2-3, significantly less than that of pure MoS_2 (over 20 layers) [40,47,48].

We further employed TEM (Figure 4) and SEM to investigate the microstructure of MoS_2/GS hybrids. As shown in Figure 4a, layered MoS_2 was highly dispersed on the surface of GS. HRTEM image displayed that MoS_2, with few-layer thickness, was highly crystalline with a lattice spacing of ca. 0.62 nm assigned to the interspacing of the (002) crystal planes (Figure 4b). Both region 1 and region 2 were covered by MoS_2, as revealed by the corresponding EDS spectra (Figure 4e and f). Noteworthy, the lattice fringe of graphene could also be clearly observed (Figure 4b). This further demonstrated that the graphitic crystalline structure of graphene was highly restored. The layer number of graphene was about 2-5, indicating graphene was highly exfoliated. As shown by the inset of Figure 4a, the ring-like mode in SAED pattern represented a polycrystalline nature of MoS_2, and can be well indexed with a pure hexagonal MoS_2 phase. In contrast, MoS_2 rods and particles about several micrometers were obtained in the absence of graphene (number of layers >20, Figure 4c and d). For pure $(NH_4)_2MoS_4$, dark brown intermediate consisting of sheets,

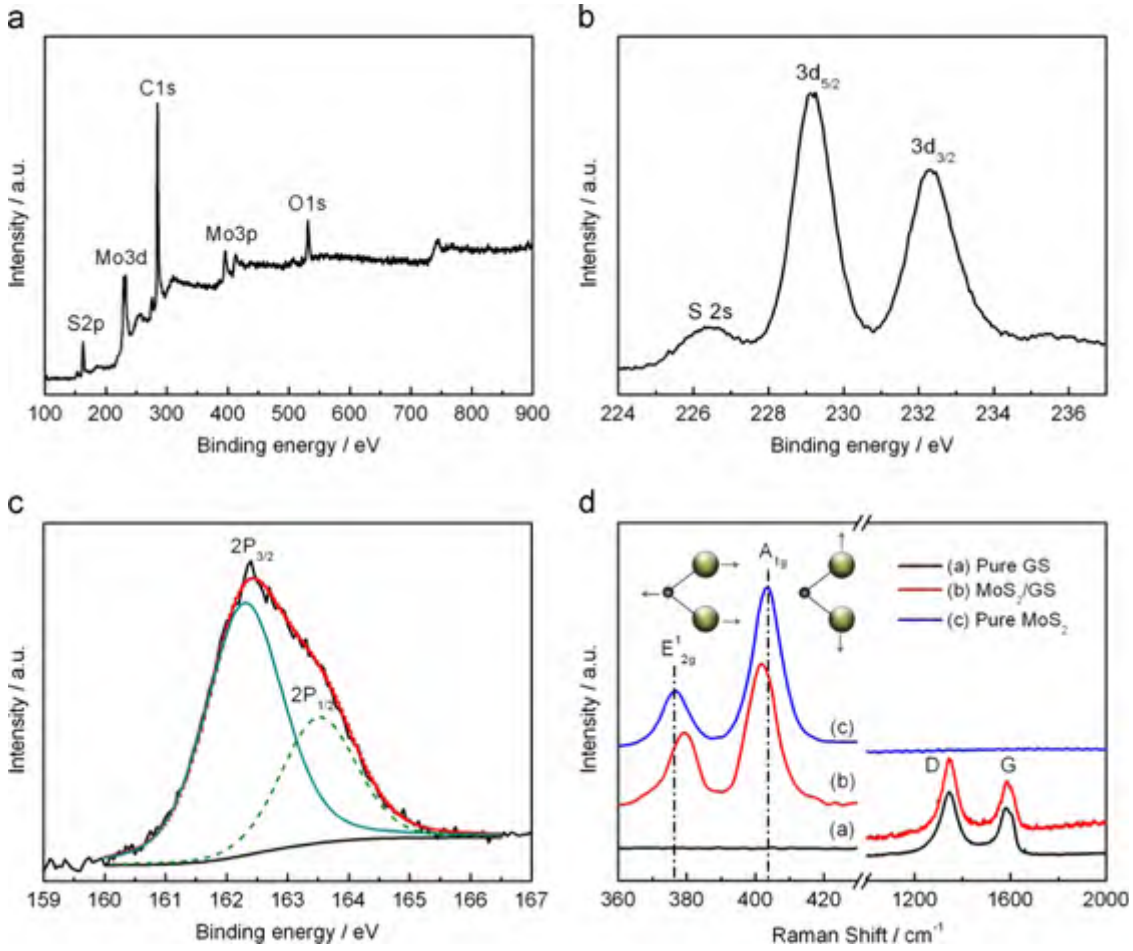

Figure 3 (a) XPS spectra of MoS_2/GS hybrid films; (b and c) the Mo3d and S2p spectrum, respectively; (d) Raman spectra of pure GS, pure MoS_2 and MoS_2/GS, the inset image in (d) shows atomic displacements of the E^1_{2g} and A_{1g} modes of MoS_2.

rods and irregular particles (about several micrometers) was obtained after continuous stirring and filtration (Figure S1a and b), which may further grow up during high temperature heat treatment due to the Ostwald ripening process. However, this was not the case with the presence of graphene. As revealed in Figure S1c and d, GO can serve as a substrate to uniformly anchor Mo-based intermediate, inhibiting its severe agglomeration and growth. During the same annealing process, Mo-based intermediate, which was spatially separated on the surface of GO, was in situ transformed into MoS_2, and thus can maintain the original excellent dispersibility. As a result, the Ostwald ripening process could be significantly restricted. Consequently, graphene not only serves as substrates to mediate the growth of MoS_2, but also effectively inhibits its overgrowth [8,49,50].

Figure 5 displays the top-view and cross-section SEM images of MoS_2/GS hybrid films. From the top view, a number of bubbles appeared on the surface of the film, which is consistent with the digital photograph (Figure 1). Closer observation showed the wrinkled and curved features of graphene (Figure 5b). As shown in Figure 5c and d, MoS_2 nanocrystals with size less than 10 nm were uniformly distributed within the hybrid film, consistent well with the TEM images. From the cross-sectional view, the thickness of the film is ~5 μm (Figure 5e). Graphene interconnected to form a 3D continuous conductive network, which functions as both a mechanical support and current collector. A magnified SEM image clearly showed the formation of an open porous network with pore sizes about several micrometers (Figure 5f). Aggregation and stacking problems are commonly observed in most of the free-standing graphene-based hybrid papers reported to date [23,25,26,51]. As a result, the unique properties of individual graphene sheets such as high accessible surface area are compromised or not achievable in the macroscopic graphene paper. In previous work, porous free-standing graphene-based films were generally constructed by template assembly methods (such as polymers [27,28,52–54] or nanoparticles [14,55]). Recently, Chen and coworker [56] used hydrazine vapor to initiate the reduction of GO, during which the rapid evolution of gaseous species could convert compact GO films into GS foams. Our condition satisfied the same two key points: (1) compact layered precursor structure and (2) rapid generation of gases during reduction. This leads to pores distributed all over the film, eventually forming the porous network. Noteworthy, this is the first demonstration that heat-induced self-generated gaseous species created flexible and free-standing hybrid films with an open porous network.

The porous structure of the MoS_2/GS hybrid films was further verified by Brunauer–Emmett–Teller (BET) specific surface area

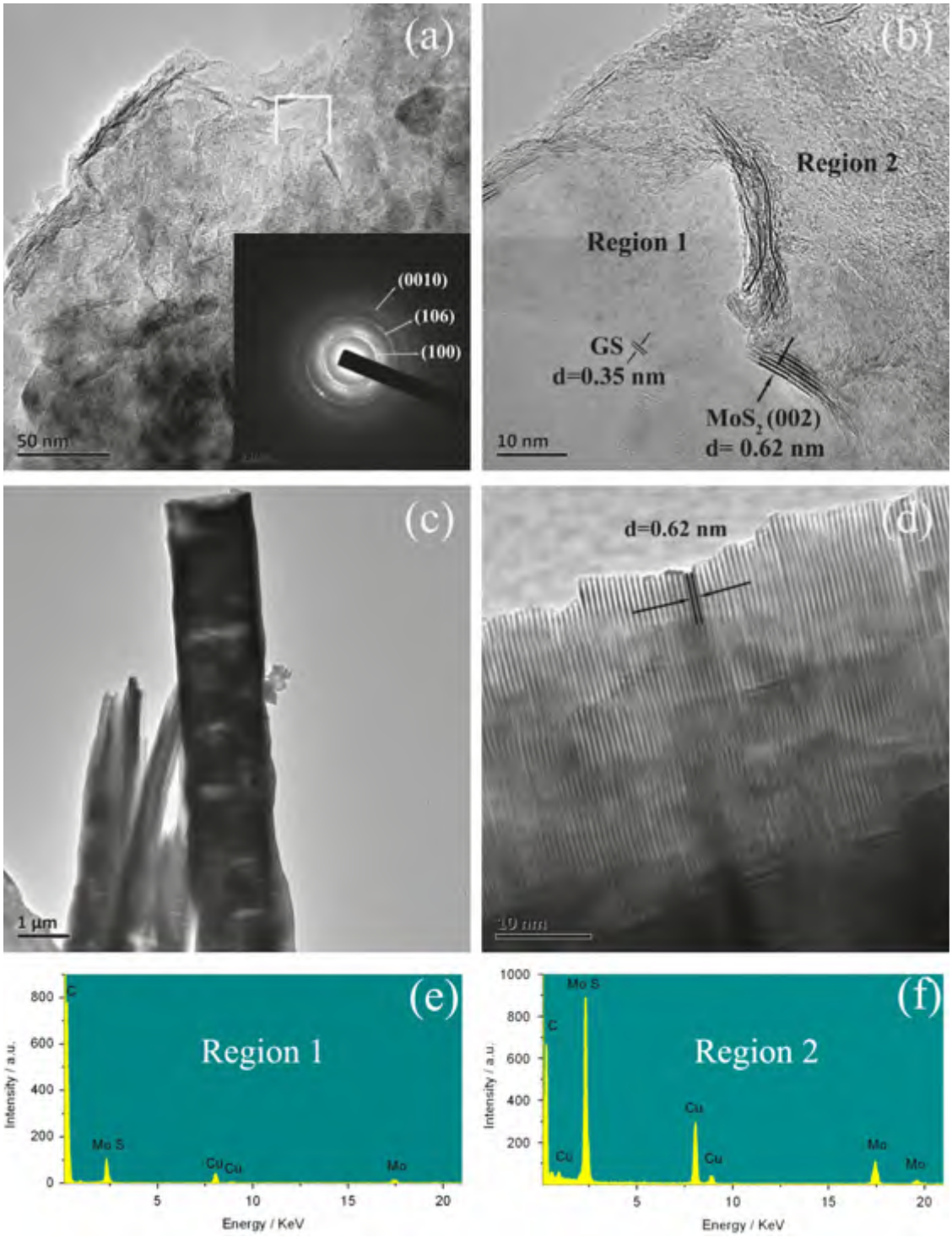

Figure 4 TEM images of MoS_2/GS hybrid (a and b) and pure MoS_2 (c and d), the inset in (a) is the corresponding SAED pattern; (e and f) EDS spectra of region 1 and region 2 in (b).

measurements (Figure S4). As shown in Figure S4a, the specific surface area of $(NH_4)_2MoS_4$/GO film was only 5.4 $m^2\,g^{-1}$, confirming its compact layered structure. However, the MoS_2/GS-II films possessed a relatively high specific surface area of 53.7 $m^2\,g^{-1}$ (Figure S4b). This further proved that heat-induced self-generated gases successfully triggered the formation of porous structure within the hybrid film. The average pore diameter was 3.6 nm. Such porous structure will facilitate the cross-plane ion diffusivity and provide more surface reaction sites, and is therefore favorable for electrochemical properties [1].

Due to the novel structures containing the ultrathin MoS_2 nanosheets, 3D highly conductive network and porous structure, our MoS_2/GS hybrid films are expected to present good performance as anode materials for LIBs. In our study, the porous graphene conductive network can act as a highly

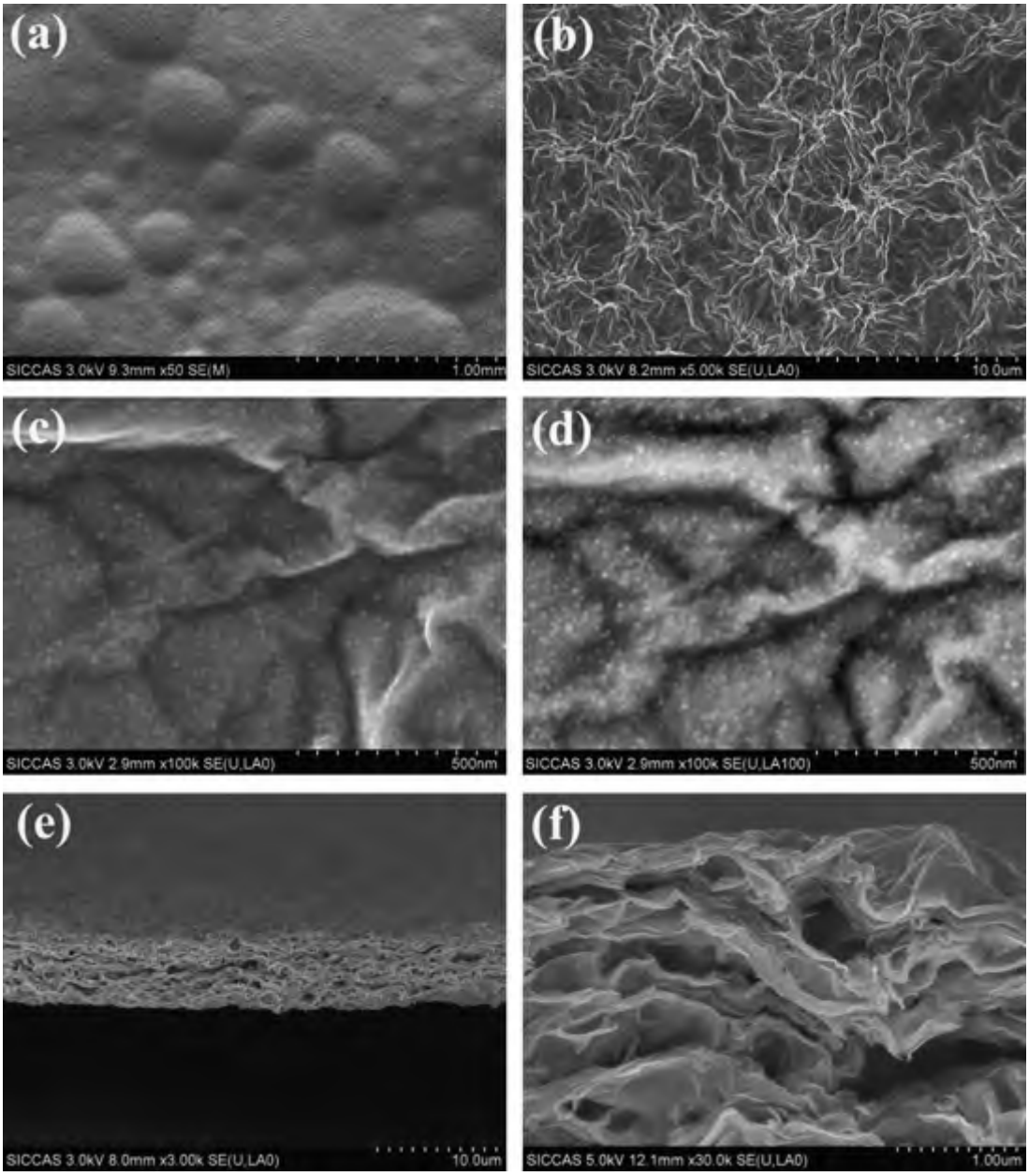

Figure 5 (a–c) the top-view SEM images of MoS_2/GS films, (d) the corresponding backscattered SEM image of (c); (e and f) the cross-section SEM images.

conductive pathway for electrons/lithium ions and current collector, without using insulating binder or conducting additive. Figure 6a shows the initial five consecutive CV curves of the MoS_2/GS electrode. In the first cathodic scan, one shoulder peak at around 0.74 V can be attributed to the phase transformation of MoS_2 from 2H (trigonal prismatic) to 1T (octahedral) Li_xMoS_2 (reaction 1) [2]. The other peak at 0.47 V was ascribed to the reduction of Mo^{4+} to Mo, accompanied by the formation of Li_2S (reaction 2) [2,8,10,11]. The whole discharge process can be expressed by the following reactions:

$$MoS_2 + xLi^+ + xe^- \rightarrow Li_xMoS_2 \quad (1)$$

$$Li_xMoS_2 + (4-x)Li^+ + (4-x)e^- \rightarrow 2Li_2S + Mo \quad (2)$$

In the first anodic scan, the anodic peak at 1.50 V corresponded to the partial oxidation of Mo to MoS_2, while the other one at 2.28 V was associated with oxidation of Li_2S to S ($Li_2S - 2e^- \rightarrow 2Li^+ + S$) [2,49]. After the first cycle, the electrode was mainly composed of Mo, S and a little amount of MoS_2 [9,49]. Accordingly, in the subsequent discharge cycles, the reduction peak at 1.78 V was indicative of the lithiation process of S to form Li_2S [2,57], another at 1.16 V was attributed to the association of Li and Mo [57]. As reported by Lemmon and coworkers, the presence of Mo metal after the first discharge can significantly improve the electronic conductivity of the whole electrode [57], while the free-standing film can restrict the diffusion of soluble polysulfide (Li_2S_8 and Li_2S_4) into electrolyte [58]. Consequently, the reversibility of lithium insertion and extraction

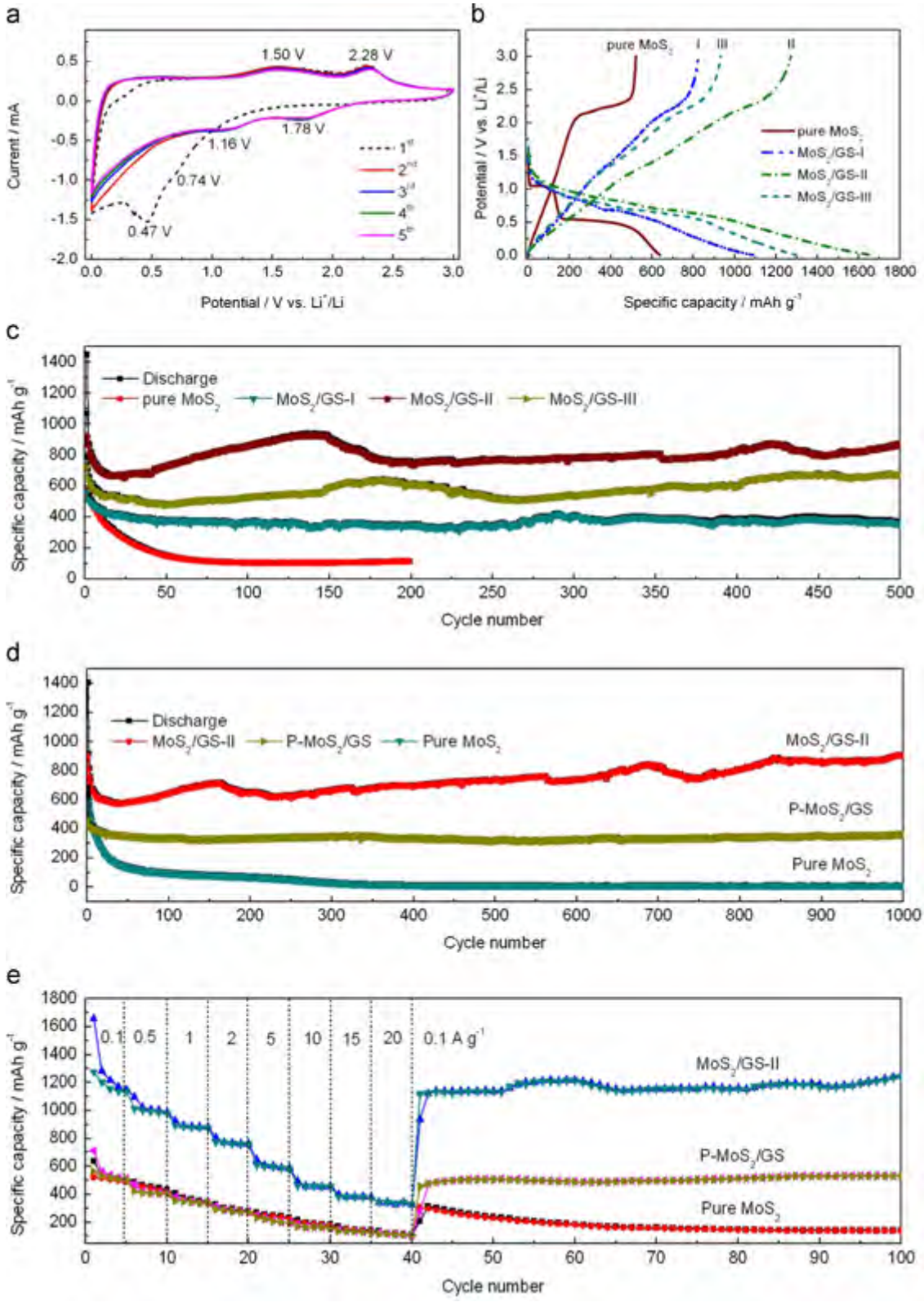

Figure 6 (a) Cyclic voltammograms for the first five cycles of MoS_2/GS electrode; (b) charge–discharge voltage profiles of MoS_2/GS electrodes and pure MoS_2 electrode at a current density of 100 mA g^{-1}; (c and d) comparative cycle performance of different electrodes at a current density of 500 and 1000 mA g^{-1}, respectively; (e) the rate capability of electrodes at different current densities. The capacity is based on the weight of the whole composite.

reactions was excellent as demonstrated by the overlapped CV curves. In the case of pure MoS_2, the peak intensity and integrated area dropped rapidly, implying a large capacity loss occurred in the lithium storage process (Figure S5). Compared with the CV curves of pure MoS_2, the shift in reduction peak potentials or changes in reduction peak shape of MoS_2/GS electrode could be caused by the overlap of electrochemical lithium storage in both MoS_2 and GS [2].

Figure 6b displays the discharge/charge curves in the first cycle of pure MoS_2 and MoS_2/GS with various MoS_2 contents, measured at a current density of 100 mA g^{-1} between 0.01-3.0 V vs. Li^+/Li. For the MoS_2/GS electrode, two plateaus at around 1.1 and 0.6 V were observed in the discharge curve, suggesting the two-step lithiation process of MoS_2; the other two at around 1.4 and 2.2 V during charge step corresponded to the partial oxidation of Mo to MoS_2 and oxidation of Li_2S to S, respectively. The discharge/charge curves of all electrodes were in accordance with the CV profiles. In the case of pure MoS_2, only one plateau was observed at ~2.2 V in the charge curve, indicating Mo could not be partially oxidized into MoS_2. It was reported that the activation energies for solid-state double decomposition reactions increases with increasing particle size [59,60]. Thus, the conversion reaction, $MoS_2 + 4Li^+ + 4e^- \rightarrow Mo + 2Li_2S$, which was partially reversible in MoS_2/GS, became irreversible for pure MoS_2 due to the big particle size. The initial discharge capacities of pure MoS_2, MoS_2/GS-I, MoS_2/GS-II and MoS_2/GS-III electrodes were 637, 1089, 1661 and 1296 mAh g^{-1}, respectively, while the initial charge capacities were 521, 825, 1276 and 933 mAh g^{-1}, respectively (based on the total weight of the hybrid). The corresponding initial coulombic efficiencies of MoS_2/GS-I, MoS_2/GS-II and MoS_2/GS-III were 75.1%, 76.8% and 72.0%, respectively. The irreversible capacity loss may be due to the electrolyte decomposition and formation of a solid electrolyte interface (SEI) layer in the discharge process [12,57]. Obviously, the specific capacity of MoS_2 was significantly improved, and MoS_2/GS-II exhibited the highest lithiation/delithiation capacities. Furthermore, the coulombic efficiency of MoS_2/GS-II was comparable or even higher than many reported literatures [11,12,57,61].

Besides higher specific capacity, MoS_2/GS electrode also showed superior cycling performance than that of pure MoS_2 electrode (Figure 6c). When cycled at 500 mA g^{-1}, the capacity of pure MoS_2 decayed significantly and retained only ~110 mAh g^{-1} after only 200 cycles. In contrast, MoS_2/GS-I, MoS_2/GS-II and MoS_2/GS-III displayed much improved capacities of 355, 867 and 669 mAh g^{-1} after 500 cycles, retaining 63.3%, 94.2% and 92.8% of their initial capacities, respectively. As demonstrated in previous studies [8,14], the ratio of high capacity active material to GS has significant effects on the dispersibility of both components, the conductivity and theoretical capacity of electrode, which will further synergistically affect the final lithium storage performance. For MoS_2/GS-I, the theoretical capacity is the lowest because the capacity of pure graphene is much lower than that of MoS_2, thus leading to the lowest capacity among the three samples. For MoS_2/GS-III, the lowest amount of GS endows the electrode the highest theoretical capacity, but with the lowest conductivity and poor dispersibility of MoS_2 simultaneously. However, MoS_2/GS-II achieves a good compromise among these three factors, and consequently, represented the highest specific capacity and the best cycle stability. Therefore, the optimal graphene content was 32%.

To further demonstrate the superiority of free-standing and binder-less electrode, MoS_2/GS-II hybrid films were also mixed with carbon black and PVDF binder, which were then coated on current collectors to prepare conventional electrodes (denoted as P-MoS_2/GS). These electrodes were tested at a higher current density of 1000 mA g^{-1} with larger numbers of cycles (Figure 6d). For pure MoS_2, the specific capacity decreased significantly and maintained only 1.9% of the initial capacity after 1000 cycles. In the case of P-MoS_2/GS, though the cycling stability was greatly improved (capacity retention was 77.2%), the specific capacity can only reach 358 mAh g^{-1} after 1000 cycles. In contrast, MoS_2/GS-II delivered a high capacity and increased to 907 mAh g^{-1} after 1000 cycles, preserving 100.6% of the initial capacity. The enhanced capacity is attributed to the formation of the gel-like polymeric layer and possibly interfacial lithium storage as well as electrochemical activation of the hybrid during the cycling process [8,11,49]. Notably, this cycle number is 50-200 times larger than those of typical battery tests. Even at an ultrahigh current density of 10000 mA g^{-1} (charging/discharging time ca. ~6 min), a capacity as high as 553 mAh g^{-1} was still retained over 7500 cycles (Figure S6). The capacity decay was as low as 0.00127% per cycle and the average coulombic efficiency achieved nearly 100% from the second cycle, manifesting an excellent prolonged cycling stability. It is demonstrated that free-standing and binder-free electrode structure indeed resulted in better active material utilization as well as an improved electrochemical performance. To the best of our knowledge, this is one of the best performing MoS_2/GS anodes reported to date in terms of long cycle life.

The high reversible lithium storage properties are also exhibited in the rate capability. As shown in Figure 6e, the hybrid electrode delivered very high capacity of 1157, 994, 880, 763 and 598 mAh g^{-1} at 0.1, 0.5, 1, 2 and 5 A g^{-1}, respectively. Even at ultrahigh current density of 10, 15 and 20 A g^{-1}, the electrode retained a capacity of 461, 379 and 344 mAh g^{-1}, respectively. This rate performance is quite remarkable in that the capacity of 344 mAh g^{-1} was achieved within ~1.0 min of charging or discharging time. Also, such rate capability is superior to that of pure MoS_2, P-MoS_2/GS and most of the published work on MoS_2/GS composite powders [2,11,50,62]. Importantly, when the current density returned to 0.1 A g^{-1} after cycling at different rates, a capacity of 1242 mAh g^{-1} was recovered in another 60 cycles. This further implied the stable structure of the hybrid film and the good reversibility. As shown in previous studies, the high rate performance highly depended on the rapid ionic and electronic diffusion and transport [63-65]. In our case, the few layered MoS_2 could shorten lithium ion and electron diffusion distance. The intimate contact and morphological compatibility between MoS_2 and GS greatly promoted interfacial lithium ion and electron transport. Meanwhile, the absence of non-conducting PVDF binder could also improve the electrode electronic conductivity. More importantly, the porous structure provided fast electronic and ionic conducting channels within the hybrid film. These unique characteristics lead to the outstanding rate capability of the free-standing and binder-free MoS_2/GS electrode.

To understand the electrochemical reaction kinetics and interfacial behavior of the hybrid electrode during the cycling process, EIS was conducted along with different charge/discharge cycles at frequencies from 100 kHz to 0.01 Hz (Figure 7). The semicircle appeared in the medium frequency range is classically assigned to the charge-transfer resistance (R_{ct}) occurring between active materials and liquid electrolyte. The straight line is attributed to the diffusion of lithium ions into electrode materials or so-called Warburg diffusion [19,62]. The fresh cell displayed a small R_{ct} of 27.0 Ω, indicating the hybrid electrode possesses a small charge-transfer resistance. After 100 cycles, R_{ct} decreased to 21.7 Ω, suggesting good electrode stability with an activation process. With prolonged cycles, R_{ct} slightly changed from 23.7 Ω at 300 cycles to 21.6 Ω at 500 cycles. This means the charge-transfer kinetics of the hybrid electrode did not degrade even after 500 cycles, demonstrating the excellent stability. Moreover, the slope showed a similar feature to the original electrode after 500 cycles, implying that facile lithium diffusion channels can be preserved during the reversible insertion/extraction process [19].

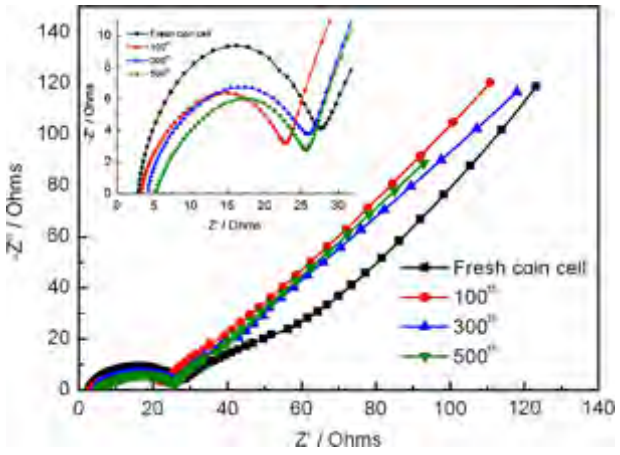

Figure 7 Nyquist plots of MoS_2/GS-II free-standing and binder-free electrode along with different charge/discharge cycles at a current density of 500 mA g^{-1}. Inset shows the enlarged spectra at high-frequency range.

In order to explore the structural stability of the cycled electrode, we further investigated the microstructure after 500 continuous cycles by SEM and TEM techniques. As shown in Figure 8a, the free-standing and binder-free electrode preserved its integrity, and few cracks were found after the cycling test. Closer observation showed a polymer/gel-like coating appeared on the surface, due to the formation of SEI. From the cross-sectional view, the hybrid film maintained the initial porous layered structure. Noteworthy, many particles with irregular shape appeared within the gaps of MoS_2/GS sheets. EDS showed the existence of F element, indicating these particles are $LiPF_6$ from electrolyte (Figure S7 and Table S2). This gave full evidence that the formation of porous structure within the hybrid film indeed facilitates the cross-plane electrolyte diffusivity, thereby providing large surface reaction sites and contributing to the improved electrochemical properties. A magnified

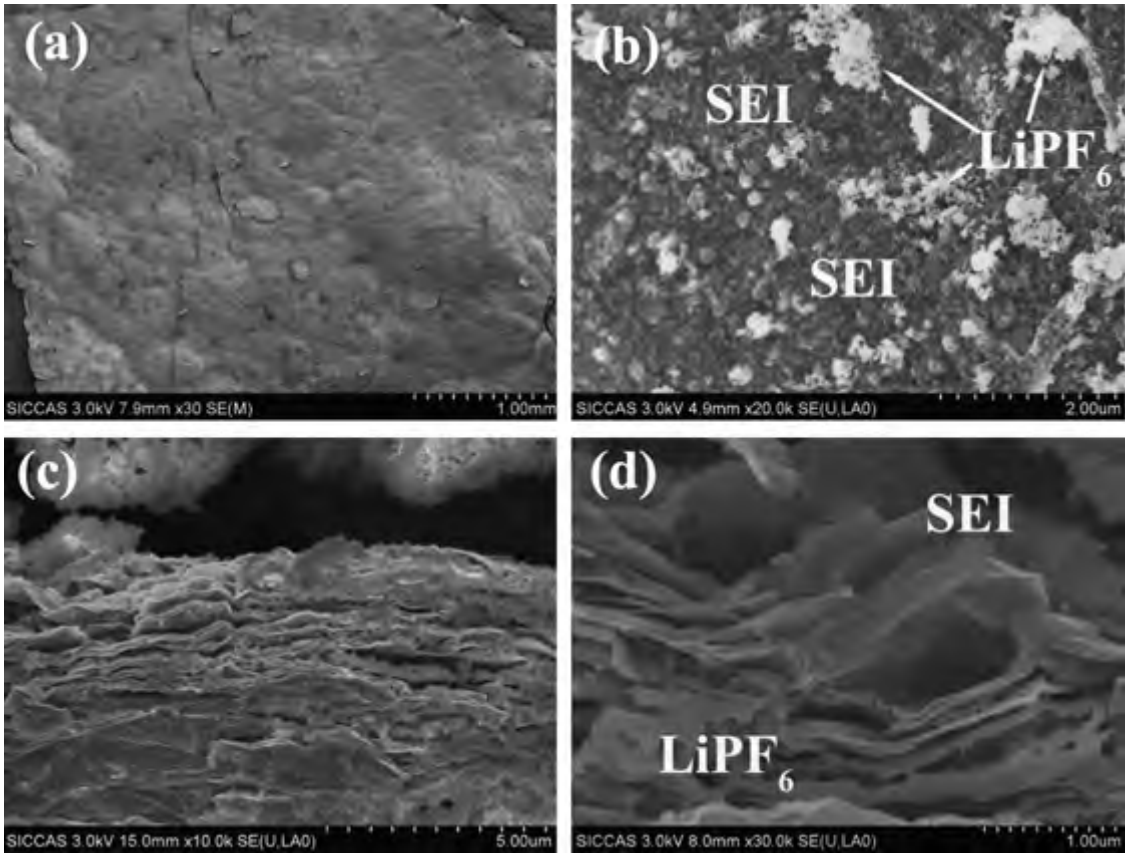

Figure 8 Top view (a and b) and cross-section SEM images (c and d) of MoS_2/GS-II hybrid film after cycling at 500 mA g^{-1}.

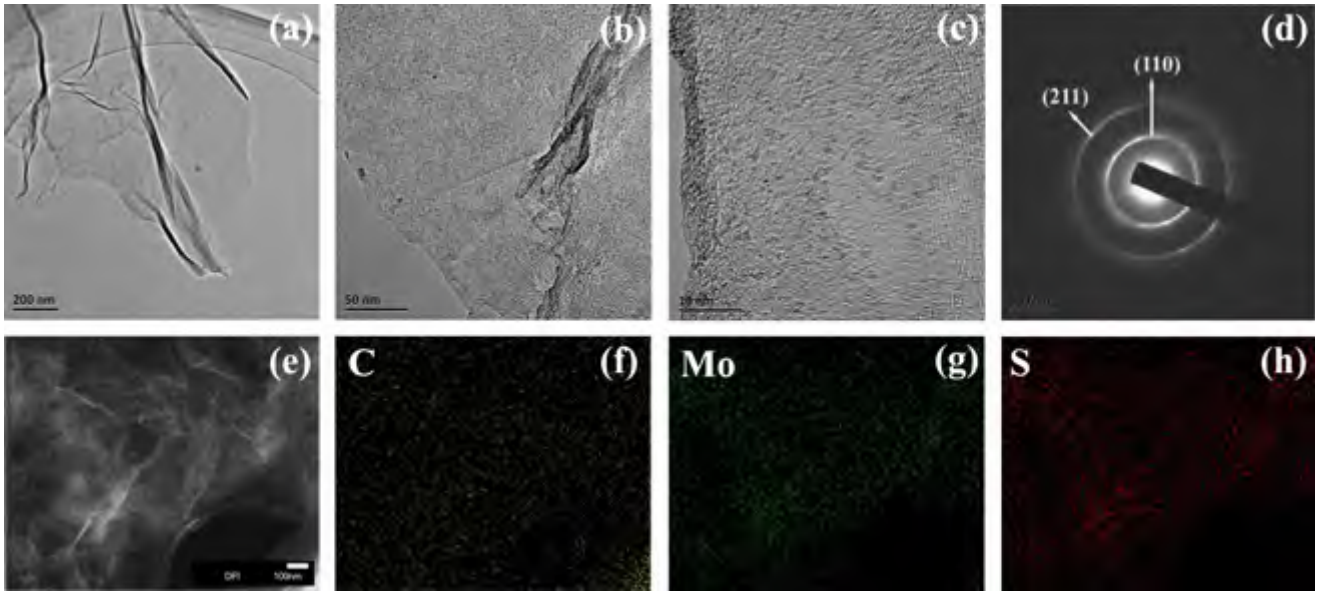

Figure 9 (a and b) TEM, (c) HRTEM images and (d) SAED pattern of MoS_2/GS hybrid film after cycling at 500 mA g^{-1} for 500 cycles, (e–h) EDS maps of C, Mo and S elements after cycling.

SEM image confirmed the generation of SEI layer on the surface of MoS_2/GS sheets.

Figure 9 displays the TEM images of the cycled hybrid film. MoS_2/GS hybrids exhibited a rippled morphology similar to that of pure graphene, and lots of ultra small particles uniformly distributed on the surface of GS (Figure 9a and b). As shown by HRTEM image, atomic clusters instead of lattice fringes of MoS_2 were detected (Figure 9c). Accordingly, it was speculated that the composition of the electrode had changed from initial MoS_2 to a mixture of Mo and S after the first cycle [10,57]. The SAED pattern verified that the atomic clusters were Mo nanocrystals (Figure 9d). This suggests the first reaction between lithium and MoS_2 was not totally reversible, thus resulting in the evolution of gel-like polymer layer and the initial capacity loss. EDS showed the atomic ratio of S to Mo element was 2.3, approaching the theoretical value of MoS_2 (Figure S8 and Table S3). The C, Mo and S element mapping further confirmed the homogenous distribution of MoS_2 on GS had been preserved even after 500 cycles (Figure 9e–h), demonstrating the aggregation of Mo nanoparticles has been well controlled.

It is well known that severe volume change and particle aggregation associated with Li^+ insertion and extraction process lead to electrode pulverization and poor cycling stability. EIS and morphology study confirmed that the persistent homogeneous distribution of both electrode components as well as its excellent structural robustness must contribute mostly to the excellent cycling stability. Additionally, the numerous pores within the hybrid film facilitate Li ions to gain access to MoS_2 efficiently, thus contributing to the high specific capacity.

Conclusions

Heat-induced rapid evolution of gaseous species successfully created flexible and free-standing MoS_2/GS hybrid films with open porous and continuously cross-linked structures. As binder-less and free-standing anode materials, the optimized hybrid film delivered high specific capacity (1276 mAh g^{-1} at 100 mA g^{-1}), excellent rate capability (994, 880 and 598 mAh g^{-1} at 0.5, 1 and 5 A g^{-1}, respectively) and extraordinary cyclic stability at high rates (preserving 100.6% of the initial capacity after 1000 cycles at 1000 mA g^{-1}). The superior electrochemical performance could be attributed to two reasons: (i) 3D flexible graphene network could enhance the conductivity of the electrode, prevent the electrochemical agglomeration of MoS_2, and maintain an integrity of the overall electrode; (ii) the porous structure of the hybrid film provided a large number of surface reaction sites and favored facile penetration of the electrolyte. EIS and morphology study showed the homogeneous distribution of both electrode components after cycling as well as the excellent structural robustness of the electrode. The present work highlights a novel strategy to synthesize porous graphene-based films, with the potential for new device designs for energy applications.

Acknowledgments

This work was supported by the 973 Project (2012CB932303), the National Natural Science Foundation of China (Grant no. 51172261).

Appendix A. Supplementary information

Supplementary data associated with this article can be found in the online version at http://dx.doi.org/10.1016/j.nanoen.2014.05.009.

Author Contributions: R. Wang and C. Xu contributed equally.

References

[1] S.Q. Chen, P. Bao, G.X. Wan, Nano Energy 2 (2013) 425–434.
[2] Z. Wang, T. Chen, W.X. Chen, K. Chang, L. Ma, G.C. Huang, D.Y. Chen, J.Y. Lee, J. Mater. Chem. A 1 (2013) 2202–2210.
[3] Y.G. Yao, L. Tolentino, Z.Z. Yang, X.J. Song, W. Zhang, Y.S. Chen, C.P. Wong, Adv. Funct. Mater. 23 (2013) 3577–3583.
[4] Y.G. Li, H.L. Wang, L.M. Xie, Y.Y. Liang, G.S. Hong, H.J. Dai, J. Am. Chem. Soc. 133 (2011) 7296–7299.
[5] Z.Y. Zeng, T. Sun, J.X. Zhu, X. Huang, Z.Y. Yin, G. Lu, Z.X. Fan, Q.Y. Yan, H.H. Hng, H. Zhang, Angew. Chem.-Int. Ed. 51 (2012) 9052–9056.
[6] H. Liu, D.W. Su, R.F. Zhou, B. Sun, G.X. Wang, S.Z. Qiao, Adv. Energy Mater. 2 (2012) 970–975.
[7] H. Hwang, H. Kim, J. Cho, Nano Lett. 11 (2011) 4826–4830.
[8] K. Chang, W.X. Chen, Acs Nano 5 (2011) 4720–4728.
[9] J.Z. Wang, L. Lu, M. Lotya, J.N. Coleman, S.L. Chou, H.K. Liu, A.I. Minett, J. Chen, Adv. Energy Mater. 3 (2013) 798–805.
[10] L.C. Yang, S.N. Wang, J.J. Mao, J.W. Deng, Q.S. Gao, Y. Tang, O.G. Schmidt, Adv. Mater. 25 (2012) 1180–1184.
[11] Y.G. Guo, X.S. Zhou, L.J. Wan, Chem. Commun. 49 (2013) 1838–1840.
[12] S.-K. Park, S.-H. Yu, S.-H. Woo, B. Quan, D.-C. Lee, M.K. Kim, Y.-E. Sung, Y.Z. Piao, Dalton Trans. 22 (2012) 2399–2405.
[13] X.S. Zhou, L.J. Wan, Y.G. Guo, Nanoscale 4 (2012) 5868–5871.
[14] R.H. Wang, C.H. Xu, J. Sun, L. Gao, C.C. Lin, J. Mater. Chem. A 1 (2013) 1794–1800.
[15] H.C. Tao, L.Z. Fan, Y.F. Mei, X.H. Qu, Electrochem. Commun. 13 (2011) 1332–1335.
[16] Z.Q. Niu, J.J. Du, X.B. Cao, Y.H. Sun, W.Y. Zhou, H.H. Hng, J. Ma, X.D. Chen, S.S. Xie, Small 8 (2012) 3201–3208.
[17] Z.S. Wu, G.M. Zhou, L.C. Yin, W. Ren, F. Li, H.M. Cheng, Nano Energy 1 (2012) 107–131.
[18] C.H. Han, M.Y. Yan, L.Q. Mai, X.C. Tian, L. Xu, X. Xu, Q.Y. An, Y.L. Zhao, X.Y. Ma, J.L. Xie, Nano Energy 2 (2013) 916–922.
[19] X.L. Jia, Z. Chen, X. Cui, Y.T. Peng, X.L. Wang, G. Wang, F. Wei, Y.F. Lu, Acs Nano 6 (2012) 9911–9919.
[20] L. Noerochim, J.Z. Wang, S.L. Chou, D. Wexler, H.K. Liu, Carbon 50 (2012) 1289–1297.
[21] J.W. Lee, S.Y. Lim, H.M. Jung, T.H. Hwang, J.K. Kang, J.W. Choi, Energy Environ. Sci. 5 (2012) 9889–9894.
[22] X. Wang, X.Q. Cao, L. Bourgeois, H. Guan, S.M. Chen, Y.T. Zhong, D.M. Tang, H.Q. Li, T.Y. Zhai, L. Li, Y. Bando, D. Golberg, Adv. Funct. Mater. 22 (2012) 2682–2690.
[23] X. Zhao, C.M. Hayner, M.C. Kung, H.H. Kung, Adv. Energy Mater. 1 (2011) 1079–1084.
[24] X. Zhou, L.-J. Wan, Y.-G. Guo, Adv. Mater. 25 (2013) 2152–2157.
[25] T. Hu, X. Sun, H.T. Sun, M.P. Yu, F.Y. Lu, C.S. Liu, J. Lian, Carbon 51 (2013) 322–326.
[26] Z.P. Li, Y.J. Mi, X.H. Liu, S. Liu, S.R. Yang, J.Q. Wang, J. Mater. Chem. 21 (2011) 14706–14711.
[27] B.G. Choi, M.H. Yang, W.H. Hong, J.W. Choi, Y.S. Huh, Acs Nano 6 (2012) 4020–4028.
[28] B.G. Choi, S.-J. Chang, Y.B. Lee, J.S. Bae, H.J. Kim, Y.S. Huh, Nanoscale 4 (2012) 5924–5930.
[29] R.S. Ruoff, X.J. Zhu, Y.W. Zhu, S. Murali, M.D. Stollers, Acs Nano 5 (2011) 3333–3338.
[30] J.S. Lee, K.H. You, C.B. Park, Adv. Mater. 24 (2012) 1084–1088.
[31] Y.G. Guo, X.S. Zhou, Y.X. Yin, L.J. Wan, J. Mater. Chem. 22 (2012) 17456–17459.
[32] X.L. Yang, K.C. Fan, Y.H. Zhu, J.H. Shen, X. Jiang, P. Zhao, C.Z. Li, J. Mater. Chem. 22 (2012) 17278–17283.
[33] W.H. Pan, M.E. Leonowicz, E.I. Stiefel, Inorg. Chem. 22 (1983) 672–678.
[34] I. Bezverkhy, P. Afanasiev, M. Lacroix, Inorg. Chem. 39 (2000) 5416–5417.
[35] W.H. Pan, M.A. Harmer, T.R. Halbert, E.I. Stiefel, J. Am. Chem. Soc. 106 (1984) 459–460.
[36] T. Weber, J.C. Muijsers, J.W. Niemantsverdriet, J. Phys. Chem. 99 (1995) 9194–9200.
[37] A. Muller, E. Krickemeyer, A. Hadjikyriacou, D. Coucouvanis, in: A.P. Ginsberg (Ed.), Inorganic Syntheses, Volume 27, John Wiley & Sons, Inc., Hoboken, NJ, USA, 2007 10.1002/9780470132586.ch9.
[38] J. Gregory, Nature 338 (1989) (182–182).
[39] Y.H. Lee, X.Q. Zhang, W.J. Zhang, M.T. Chang, C.T. Lin, K.D. Chang, Y.C. Yu, J.T.W. Wang, C.S. Chang, L.J. Li, T. W. Lin, Adv. Mater. 24 (2012) 2320–2325.
[40] K.-K. Liu, W.J. Zhang, Y.-H. Lee, Y.-C. Lin, M.-T. Chang, C.-Y. Su, C.-S. Chang, H. Li, Y.M. Shi, H. Zhang, C.-S. Lai, L.-J. Li, Nano Lett. 12 (2012) 1538–1544.
[41] S.-Y. Tai, C.-J. Liu, S.-W. Chou, F.S.-S. Chien, J.-Y. Lin, T.-W. Lin, J. Mater. Chem. 22 (2012) 24753–24759.
[42] R.H. Wang, Y. Wang, C.H. Xu, J. Sun, L. Gao, Rsc Adv. 3 (2013) 1194–1200.
[43] J. Sun, R.H. Wang, C.H. Xu, Y.Q. Liu, L. Gao, C.C. Lin, Nanoscale 5 (2013) 6960–6967.
[44] D. Li, M.B. Muller, S. Gilje, R.B. Kaner, G.G. Wallace, Nat. Nanotechnol. 3 (2008) 101–105.
[45] J.N. Coleman, M. Lotya, A. O'Neill, S.D. Bergin, P.J. King, U. Khan, K. Young, A. Gaucher, S. De, R.J. Smith, I.V. Shvets, S.K. Arora, G. Stanton, H.Y. Kim, K. Lee, G.T. Kim, G.S. Duesberg, T. Hallam, J.J. Boland, J.J. Wang, J.F. Donegan, J.C. Grunlan, G. Moriarty, A. Shmeliov, R.J. Nicholls, J.M. Perkins, E.M. Grieveson, K. Theuwissen, D.W. McComb, P.D. Nellist, V. Nicolosi, Science 331 (2011) 568–571.
[46] S. Ghatak, A.N. Pal, A. Ghosh, Acs Nano 5 (2011) 7707–7712.
[47] C. Lee, H. Yan, L.E. Brus, T.F. Heinz, J. Hone, S. Ryu, Acs Nano 4 (2010) 2695–2700.
[48] H.S. Lee, S.W. Min, Y.G. Chang, M.K. Park, T. Nam, H. Kim, J.H. Kim, S. Ryu, S. Im, Nano Lett. 12 (2012) 3695–3700.
[49] K. Chang, D.S. Geng, X.F. Li, J.L. Yang, Y.J. Tang, M. Cai, R.Y. Li, X.L. Sun, Adv. Energy Mater. 3 (2013) 839–844.
[50] H.L. Yu, C. Ma, B.H. Ge, Y.J. Chen, Z. Xu, C.L. Zhu, C.Y. Li, Q. Ouyang, P. Gao, J.Q. Li, C.W. Sun, L.H. Qi, Y.M. Wang, F.H. Li, Chem. – Eur. J. 19 (2013) 5818–5823.
[51] A. Sumboja, C.Y. Foo, X. Wang, P.S. Lee, Adv. Mater. 25 (2013) 2809–2815.
[52] Q. Wu, Y.X. Xu, Z.Y. Yao, A.R. Liu, G.Q. Shi, Acs Nano 4 (2010) 1963–1970.
[53] X.C. Chen, W. Wei, W. Lv, F.Y. Su, Y.B. He, B.H. Li, F.Y. Kang, Q.H. Yang, Chem. Commun. 48 (2012) 5904–5906.
[54] S.H. Lee, H.W. Kim, J.O. Hwang, W.J. Lee, J. Kwon, C.W. Bielawski, R.S. Ruoff, S.O. Kim, Angew. Chem.-Int. Ed. 122 (2010) 10282–10286.
[55] X.D. Huang, K. Qian, J. Yang, J. Zhang, L. Li, C.Z. Yu, D.Y. Zhao, Adv. Mater. 24 (2012) 4419–4423.
[56] Z.Q. Niu, J. Chen, H.H. Hng, J. Ma, X.D. Chen, Adv. Mater. 24 (2012) 4144–4150.
[57] J. Xiao, X.J. Wang, X.Q. Yang, S.D. Xun, G. Liu, P.K. Koech, J. Liu, J.P. Lemmon, Adv. Funct. Mater. 21 (2011) 2840–2846.
[58] J. Jin, Z.Y. Wen, G.Q. Ma, Y. Lu, Y.M. Cui, M.F. Wu, X. Liang, X.W. Wu, Rsc Adv. 3 (2013) 2558–2560.
[59] P.C. Lian, X.F. Zhu, S.Z. Liang, Z. Li, W.S. Yang, H.H. Wang, Electrochim. Acta 56 (2011) 4532–4539.
[60] D.N. Wang, J.L. Yang, X.F. Li, D.S. Geng, R.Y. Li, M. Cai, T.-K. Sham, X.L. Sun, Energy Environ. Sci. 6 (2013) 2900–2906.
[61] S. Ding, J.S. Chen, X.W. Lou, Chem. – Eur. J. 17 (2011) 13142–13145.
[62] X.H. Cao, Y.M. Shi, W.H. Shi, X.H. Rui, Q.Y. Yan, J. Kong, H. Zhang, Small 9 (2013) 3433–3438.

[63] X.L. Huang, R.Z. Wang, D. Xu, Z.L. Wang, H.G. Wang, J.J. Xu, Z. Wu, Q.C. Liu, Y. Zhang, X.B. Zhang, Adv. Funct. Mater. 23 (2013) 4345–4353.
[64] W.F. Chen, S.R. Li, C.H. Chen, L.F. Yan, Adv. Mater. 23 (2011) 5679–5683.
[65] Z.L. Wang, D. Xu, H.G. Wang, Z. Wu, X.B. Zhang, Acs Nano 7 (2013) 2422–2430.

Ronghua Wang received her B.S. degree from Qingdao University of Science & Technology in 2009, and Ph.D. degree from Shanghai Institute of Ceramics, Chinese Academy of Sciences in 2014. Her current research area includes lithium-ion batteries, supercapacitors and stretchable energy storage devices.

Chaohe Xu received his B.S. degree from Tianjin University in 2007, and Ph.D. degree from Shanghai Institute of Ceramics, Chinese Academy of Sciences in 2012. His current research area includes lithium-ion batteries, metal-air batteries, electrocatalysts, and supercapacitors.

Jing Sun received her M.S. from Changchun Institute of Applied Chemistry and Ph.D. degrees from Shanghai Institute of Ceramics in 1994 and 1997, respectively. Then she joined Shanghai Institute of Ceramics (SICCAS). She spent one year as visiting scientist in Institute for Surface Chemistry in Stockholm (YKI) between 1999 and 2000 and as a JSPS fellow in National Institute of Advanced Science and Technology (AIST) in Japan during 2002–2004. She has been appointed as a Professor in SICCAS since 2005. She is heading a research group of 20 graduate students and researchers and her current research interests include low dimensional carbon materials (including carbon nanotubes and graphene) and their composites, novel photovoltaic devices based on inorganic and organic materials, nanotubes, nanowires, and lithium ion battery materials. She has published over 150 peer-reviewed journal articles, one book and filed 15 patents in China.

Yangqiao Liu has received her B.S. degree from East China University of Science and Technology in 1993, M.S. degree from Dalian University of Technology in 1996 and Ph.D. degree from Shanghai Institute of Ceramics, Chinese Academy of Sciences (SICCAS) in 2001, respectively. She is currently a professor at the State Key Laboratory of High Performance Ceramics and Superfine Microstructures in SICCAS. She was awarded the "Shanghai Rising Star" in 2008. She has authored more than 70 scientific articles. Her research interests include energy storage materials, solar cell materials and devices, carbon nanotube and graphene-based composite materials.

LianGao received his M.S. and Ph.D. degrees from Shanghai Institute of Ceramics, Chinese Academy of Sciences in 1981 and 1986. He is a Fellow of the American Ceramic Society and an Academician of the World Academy of Ceramics. He was awarded Prize for Scientific and Technological Progress from HO LEUNG HO LEE Foundation in 2010. He has a Distinguish Professor position at Shanghai Jiao Tong University now.

Heliang Yao received his B.S. degree from East China University of Science and Technology. He is currently an engineer in Shanghai Institute of Ceramics, Chinese Academy of Sciences. His current research area includes microstructures and properties of materials by transmission electron microscope, especially the relationship between the two.

Chucheng Lin is currently a primary engineer in the Shanghai Institute of Ceramics, Chinese Academy of Sciences.His current research area includes SEM and EPMA testing work, accumulated rich experience in material microstructures and micro-ingredients characterization.